PAPER • OPEN ACCESS

Impact of eccentricity and mean anomaly in numerical relativity mergers

View the article online for updates and enhancements.

Impact of eccentricity and mean anomaly in numerical relativity mergers

Peter James Nee[1,*] , **Aldo Gamboa**[1] , **Harald P Pfeiffer**[1] ,
Lorenzo Pompili[1] , **Antoni Ramos-Buades**[2] ,
Vijay Varma[3] , **Michael Boyle**[4] ,
Alessandra Buonanno[1,5] , **Raffi Enficiaud**[1] ,
Lawrence E Kidder[4] **and Mark A Scheel**[6]

[1] Max Planck Institute for Gravitational Physics (Albert Einstein Institute), Am Mühlenberg 1, Potsdam 14476, Germany
[2] Departament de Física, Universitat de les Illes Balears, IAC3 – IEEC, Crta. Valldemossa km 7.5, E-07122 Palma, Spain
[3] Department of Mathematics, Center for Scientific Computing and Data Science Research, University of Massachusetts, Darmouth, MA 02747, United States of America
[4] Cornell Center for Astrophysics and Planetary Science, Cornell University, Ithaca, NY 14853, United States of America
[5] Department of Physics, University of Maryland, College Park, MD 20742, United States of America
[6] Theoretical Astrophysics 350-17, California Institute of Technology, Pasadena, CA 91125, United States of America

E-mail: peter.nee@aei.mpg.de

Abstract

Accurate modelling of black hole (BH) binaries is critical to achieve the science goals of gravitational-wave detectors. Modelling such configurations relies strongly on calibration to numerical-relativity (NR) simulations. Binaries on quasi-circular orbits have been widely explored in NR, however, coverage of the broader nine-dimensional parameter space, including orbital eccentricity, remains sparse. This article develops a new procedure to control orbital eccentricity of binary BH (BBH) simulations that enables choosing initial data

---

[*] Author to whom any correspondence should be addressed.

parameters with precise control over eccentricity and mean anomaly of the subsequent evolution, as well as the coalescence time. We then calculate several sequences of NR simulations that nearly uniformly cover the two-dimensional eccentricity–mean anomaly space for equal mass, non-spinning BBHs. We demonstrate that, for fixed eccentricity, many quantities related to the merger dynamics of BBHs show an oscillatory dependence on mean anomaly. The amplitude of these oscillations scales nearly linearly with the eccentricity of the system. We find that for the eccentricities explored in this work, the magnitude of deviations in various quantities such as the merger amplitude and peak luminosity can approach $\sim$5% of their quasi-circular value. We use our findings to explain eccentric phenomena reported in other studies. We also show that methods for estimating the remnant mass employed in the effective-one-body approach exhibit similar deviations, roughly matching the amplitude of the oscillations we find in NR simulations. This work is an important step towards a complete description of eccentric BBH mergers, and demonstrates the importance of considering the entire two-dimensional parameter subspace related to eccentricity.

Keywords: numerical relativity, black holes, eccentricity and mean anomaly

1. Introduction

By the end of the fourth observing run of the LIGO-Virgo-KAGRA network of gravitational-wave (GW) detectors, it is expected that the number of detected binary black hole (BBH) events will exceed 200 [1–6]. In order to both detect potential events, as well as to ascertain their properties via parameter estimation [4, 7–10], it is essential that we have accurate waveform models across the entire BBH parameter space. This necessity only becomes more drastic when considering future, next-generation detector missions such as Einstein Telescope, LISA, and Cosmic Explorer [11–14], which will not only be more sensitive (and so more prone to bias due to waveform systematics), but will also cover new frequency bands, opening up the possibility to detect BBH events from new formation channels [15–17].

While many waveform models leverage analytic prescriptions or perturbative approaches, almost all modern waveform models rely on calibration to numerical-relativity (NR) simulations (e.g. [18–20]) or are directly constructed from NR simulations [21]. This calibration can only be effective in regions of parameter space with sufficient simulation coverage. To date, much of the focus of NR simulations has been on quasi-circular systems, representing a 7 dimensional subspace of possible configurations. This is natural, as orbital eccentricity is radiated away during the inspiral of a binary [22], and so by the time the system enters current detectors' frequency bands it is typically well-described by a quasi-circular system. Still, an understanding of eccentricity is vital for several science goals; to ensure that if there are eccentric signals we can properly identify them [23–26], to explore the formation scenarios for different binary systems [17, 27–32], as well as to disambiguate eccentric effects from potential deviations of General Relativity [33–35]. To this end, there are on-going efforts to build waveform models for eccentric systems [36–41]. However, most waveform models that do allow for orbital eccentricity in the inspiral still assume a quasi-circular merger model, with the exception being `NRSur2dq1Ecc` [36]. As such, both the calibration to NR and the assessment of these merger models requires extending our coverage to the eccentric parameter space.
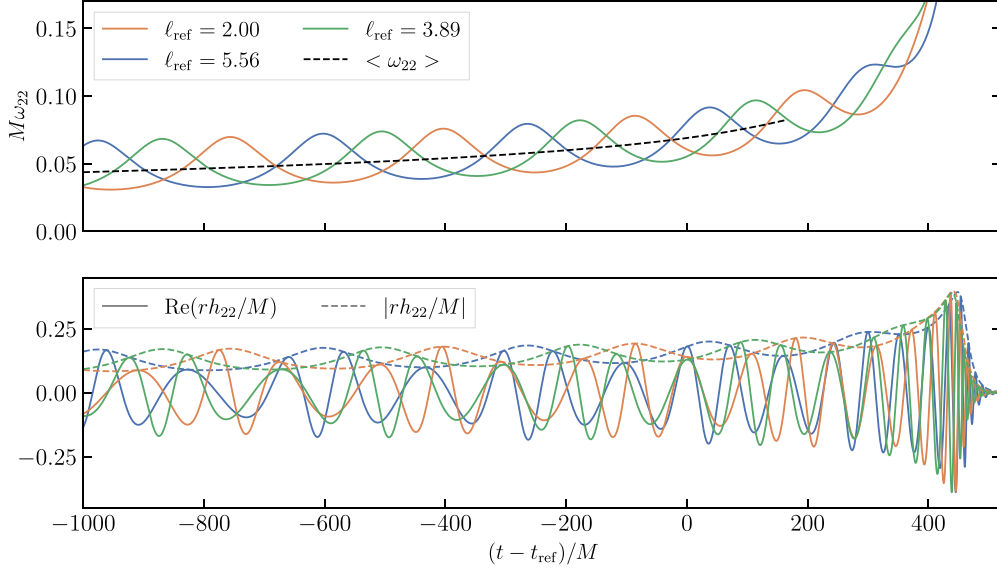
Figure 1. Importance of mean anomaly. Top panel: instantaneous GW frequency $\omega_{22}(t)$ for three NR simulations. The maxima and minima of these curves share common envelopes, indicating that these systems have the same eccentricity, and differ only in their mean anomaly. Note that all three systems share the same orbit-averaged frequency throughout their inspiral, plotted as the black dashed curve. Bottom panel: a representative GW mode, with phasing aligned at the time at which the orbit averaged frequency of the $(2, 2)$ mode $\langle \omega_{22} \rangle = 0.069/M$. While the systems accumulate the same overall number of GW cycles, the amplitude- and phase-modulations differ. This plot zooms into the merger part of the NR simulations and the full simulations are visible in figure 5.

At the same time, several NR groups have begun to expand into this part of the parameter space [36, 42–53]. However, relaxing the quasi-circular restriction not only introduces a parameter describing the eccentricity of the system (namely, the eccentricity), but also a parameter describing its phasing (typically referred to as the anomaly, see figure 1). While these serve as excellent exploratory studies, to the authors' knowledge, no complete study accounting for both eccentric parameters has been performed thus far. As such, coverage of this two-dimensional parameter space remains haphazard at best (see figure 3 of [36] for one such example).

While controlling the eccentricity of a simulation is a difficult problem in its own right [54, 55], controlling the anomaly at an arbitrary reference epoch proves even more challenging because for eccentric binary systems, the length of the simulation before the black holes (BHs) coalesce (referred to as the time to merger) has a much more sensitive dependence on the initial conditions compared to their quasi-circular counterparts. This sensitivity makes efficient exploration of eccentric binaries challenging. Therefore, to access such a complete study requires improvements upon our current eccentricity control methods.

In this work, we address two problems: first, we propose a new eccentricity control method, which is based on the gravitational waveforms and utilises state-of-the-art eccentric waveform models. This new method not only allows exceptional control over the eccentricity of the binary, but also over the length of the simulations, which in turn enables targeting of specific values of the anomaly parameter. Second, we use this method to present the first complete

exploration of the impact of both eccentricity and mean anomaly on several merger-related quantities, such as the peak of the strain and the remnant BH parameters. We demonstrate that many quantities have an oscillatory dependence on the mean anomaly, with the magnitude of these oscillations scaling roughly linearly with eccentricity. Using this information, we are able to explain features seen in previous eccentric studies. Finally, we show that some of these results may actually be accessible via analytic methods, using the SEOBNRv5EHM eccentric waveform model [38, 56].[7]

This paper is organised as follows: in section 2, we lay out several definitions used throughout this work, as well as our new waveform-based eccentricity control. In section 3, we demonstrate the effectiveness of this eccentricity control procedure, and use it to generate several sequences of eccentric simulations, which we use to assess the impact of eccentricity and mean anomaly. Finally, in section 4, we summarise our results, and discuss future avenues of research.

2. Methods

2.1. Definitions

To avoid any gauge/definition ambiguities, we will define both eccentricity and mean anomaly directly from the gravitational waveform using the package gw_eccentricity [50, 58]. One first decomposes the complex waveform $h = h_+ - ih_\times$ into a sum of spin-weighted spherical harmonics,

$$h(t, \iota, \varphi_0) = \sum_{\ell=2}^{\ell=\infty} \sum_{m=-\ell}^{m=\ell} h_{\ell m}(t) \, _{-2}Y_{\ell m}(\iota, \varphi_0), \tag{1}$$

where ι and φ_0 are the polar and azimuthal angles on the sky in the source frame, and $_{-2}Y_{\ell m}$ are the $s = -2$ spin-weighted spherical harmonics. This study is largely restricted to binaries without orbital plane precession, and $\iota = 0$ corresponds to the direction orthogonal to the orbital plane. Each mode $h_{\ell m}$ is further decomposed into a real amplitude and a real phase:

$$h_{\ell m}(t) = A_{\ell m}(t) e^{-i\phi_{\ell m}(t)}. \tag{2}$$

Following [50, 58], we introduce the frequency of h_{22} as $\omega_{22} = \mathrm{d}\phi_{22}/\mathrm{d}t$, and define the eccentricity of the system as the envelope of ω_{22}, i.e.

$$e_{\mathrm{gw}}(t) = \cos(\Psi/3) - \sqrt{3}\sin(\Psi/3), \tag{3}$$

where

$$\Psi = \arctan\left(\frac{1 - e_{\omega_{22}}^2}{2e_{\omega_{22}}}\right), \quad e_{\omega_{22}}(t) = \frac{\sqrt{\omega_{22}^{\mathrm{p}}(t)} - \sqrt{\omega_{22}^{\mathrm{a}}(t)}}{\sqrt{\omega_{22}^{\mathrm{p}}(t)} + \sqrt{\omega_{22}^{\mathrm{a}}(t)}}, \tag{4}$$

---

[7] The SEOBNRv5EHM waveform model is publicly available through the Python package pySEOBNR (https://waveforms.docs.ligo.org/software/pyseobnr) [57].

and $\omega_{22}^{\mathrm{a/p}}(t)$ are smooth interpolants of the $(2,2)$ mode frequency at apastron/periastron. For a time interval between successive periastron passages $t_i^{\mathrm{p}} < t < t_{i+1}^{\mathrm{p}}$, i.e. between maxima of ω_{22}, the mean anomaly is defined as

$$\ell_{\mathrm{gw}}(t) = 2\pi \, \frac{t - t_i^{\mathrm{p}}}{t_{i+1}^{\mathrm{p}} - t_i^{\mathrm{p}}},\tag{5}$$

where t_i^{p} is the time of the i-th periastron passage. Note that $\ell_{\mathrm{gw}}(t)$ is essentially a piecewise linear function in time, which increases from 0 to 2π between each periastron passage. We will omit the subscript 'gw' for the rest of this work.

As should be clear from the above formulae, both the eccentricity and mean anomaly of a given system are functions of time. As such, it is important to specify *where* in the waveform we are defining eccentricity and mean anomaly when comparing systems. This is typically either done at some reference time t_{ref}, or at some reference orbit-averaged frequency $\langle\omega_{22}\rangle(t)$, which we define as a smooth interpolant of

$$\langle\omega_{22}\rangle_i = \frac{1}{t_{i+1}^{\mathrm{p}} - t_i^{\mathrm{p}}} \int_{t_i^{\mathrm{p}}}^{t_{i+1}^{\mathrm{p}}} \omega_{22}(t) \, \mathrm{d}t = \frac{\phi_{22}\left(t_{i+1}^{\mathrm{p}}\right) - \phi_{22}\left(t_i^{\mathrm{p}}\right)}{t_{i+1}^{\mathrm{p}} - t_i^{\mathrm{p}}}.\tag{6}$$

Throughout this work we will make use of both reference time and reference frequencies: for comparing systems of the same eccentricity we use reference frequencies, while comparing across eccentricities we will use reference times. We will use subscripts to indicate when a quantity is defined (e.g. ℓ_{-700M} represents the mean anomaly $700M$ before merger, while $\ell_{0.03/M}$ would be the mean anomaly when $\langle\omega_{22}\rangle = 0.03/M$). Additionally, we make frequent use of an orbit averaged frequency of $\langle\omega_{22}\rangle = 0.069/M$, corresponding to an epoch near merger. For brevity, we will use the subscript 'ref' (e.g. ℓ_{ref} and t_{ref}) to denote quantities evaluated at this epoch.

As will be discussed in section 3, the choice of exactly where in the inspiral to define the reference epoch is important when studying the impact of mean anomaly on merger dynamics. The reason is that mean anomaly cycles through many periods during the inspiral (once per radial period), and so even a small secular dephasing between two runs can lead to dramatically different mean anomaly values. In contrast, eccentricity is slowly and monotonically decaying, and a change in reference epoch for the definition of eccentricity will primarily result in a re-scaling of all eccentricities that respects their ordering (for constant BH parameters). However, when comparing across systems of varying BH parameters, one could have that the $e_i(t)$ curves cross, and so the choice of reference epoch becomes more important. As we will focus on equal mass non-spinning systems in this work, we leave careful consideration of the reference epoch for defining eccentricity to future work.

Figure 1 gives a more intuitive picture of how eccentricity and mean anomaly parameterise a system. We plot the evolution of ω_{22} for three sample NR simulations (all with mass-ratio $q = 1$, both BHs non-spinning). As equation (3) depends only on the apastron and periastron frequencies (i.e. the envelopes of the frequency), it should be clear that these three simulations share the same $e(t)$. As such, a second parameter is required to distinguish between these simulations, the 'phase' of the radial orbit. This is precisely the mean anomaly $\ell(t)$.

All numerical simulations in this work were carried out using the Spectral Einstein Code (SpEC) [59] developed by the Simulating eXtreme Spacetimes (SXS) collaboration. SpEC employs a multi-domain spectral discretisation [60–63] to solve a first-order representation of the generalised harmonic system [64]. Excision surfaces are placed within apparent horizons

[61–63, 65], and constraint-preserving boundary conditions are used for the outer boundaries [64, 66, 67]. Initial data is constructed using Spells [68, 69], which solves the extended conformal-thin sandwich equations [70–72].

2.2. Waveform-based eccentricity control

The initial data of a NR simulation determines the properties of the system. In SpEC, initial data is specified through mass-ratio $q = m_1/m_2 \geqslant 1$ and BH spins $\vec{\chi}_{1,2}$, where the subscript labels the two BHs. In this paper, we will largely restrict our focus to BH spins parallel to the orbital angular momentum (which in turn is parallel to the $\hat{z}$-axis), so that $\vec{\chi}_1 = \hat{z}\chi_i$ where $\chi_i \in [-1, 1]$ represents the projection of $\vec{\chi}_i$ onto the orbital angular momentum vector. In addition to mass-ratio q and spins χ_i, one must also specify:

 (i) the initial coordinate separation D_0,
 (ii) the initial orbital frequency Ω_0, and
(iii) the initial expansion $\dot{a}_0$, defined as the initial in-going velocity divided by the initial separation v_r/D_0.

These three values encode the orbital properties (eccentricity & radial phase) as well as the merger time T_{merger}, which we define as the time of the peak of A_{22}. Our goal is to obtain precise control over mean anomaly, eccentricity, and merger time. As such, we need a procedure to obtain initial parameters D_0, Ω_0 and $\dot{a}_0$ that correspond to a NR simulation with the desired initial eccentric parameters (e_0, ℓ_0), and time to merger T_{merger}.

As a first step we will restrict ourselves to construct initial data only at apastron. Because of the larger separation and smaller velocities of the BHs at apastron, junk radiation [73] is reduced; moreover, this choice meshes well with technical restrictions of SpEC which limit by how much the separation can increase during an evolution [74]. We note that starting at apastron does not limit our ability to reach any physically possible configuration. For instance, we achieve all three simulations shown in figure 1 with initial data at apastron by suitably changing D_0, Ω_0, and $\dot{a}_0$ so that the subsequent simulations have the same eccentricity (at a reference epoch) but slightly different durations between initial data and merger. In section 3.1, we will use this approach to systematically explore the mean anomaly parameter space.

We furthermore aim for an iterative procedure to adjust our initial conditions: Based on evolutions lasting a few orbits, we aim to adjust our initial conditions, such that a subsequent evolution is closer to the desired configuration. Many such iterative eccentricity control procedures have been employed to date [54, 55, 75–80], however we shall improve on those in two ways: First, we will use the gravitational waveform in our adjustment procedure, in order to eliminate the coordinate-dependence inherent in procedures that use the coordinate trajectories of the BHs [54, 55, 75, 77, 79, 80]. Second, in our updating step, we will utilise state-of-the-art waveform models for eccentric BBH, rather than using a fitting function based on ad hoc choices (e.g. [75, 77]) or post-Newtonian inspired approximations [54]. Specifically, we employ SEOBNRv5EHM [38, 56], an aligned-spin, effective-one-body (EOB) model for eccentric BBH systems. SEOBNRv5EHM parameterises its orbit differently to NR initial data, namely with

  (i) initial eccentricity e_0,

 (ii) initial relativistic anomaly ζ_0,[8] and

(iii) initial orbit-averaged orbital frequency $\langle\Omega\rangle_0$.

The EOB model internally translates these quantities through a root-finding procedure into the actual initial conditions for the EOB dynamics evolution: separation r_0, instantaneous orbital frequency ω_0, and radial momentum p_r.

Our task is now to combine SEOBNRv5EHM with short NR simulations to achieve our target configuration with initial eccentricity e_0^{target} and time to merger $T_{\text{merger}}^{\text{target}}$. We seek an iterative procedure that ultimately yields NR initial-data parameters $(D_0, \Omega_0, \dot{a}_0)$ for our target configuration. Our eccentricity control method begins by constructing a first NR initial data as a seed for the subsequent iterative procedure:

  (i) Fix $\zeta_0 = 0$, and perform a root find in the EOB initial parameters $(e_0, \langle\Omega\rangle_0)$ to find the EOB waveform with the desired eccentricity and waveform length.

 (ii) Extract the initial dynamical quantities from the EOB model (r_0, ω_0, p_r).

(iii) Set the NR initial-data parameters to $D_0 = r_0 - M$, $\Omega_0 = \omega_0$ and $\dot{a}_0 = p_r/r_0$.

Now that we have seed NR initial conditions, we can begin the actual iterative procedure:

 (iv) Construct the NR initial-data set for $(D_0, \Omega_0, \dot{a}_0)$, and evolve for three radial periods up to a time t_{max}.

  (v) Extract the gravitational waveform from the NR simulation. We use a waveform extracted at a finite radius (typically $r \approx 300M$), discard data for $t < t_{\text{junk}}$ which is contaminated by junk radiation, and calculate the amplitude of the $(2,2)$ mode, $A_{22}^{\text{NR}}(t)$. Figure 2 plots an exemplary $A_{22}^{\text{NR}}(t)$ obtained in this way; because we remove the initial junk-radiation phase, the data starts somewhat after an apastron passage, i.e. somewhat after a minimum in $A_{22}^{\text{NR}}(t)$.

 (vi) Find the SEOBNRv5EHM waveform that best matches A_{22}^{NR}. In this step, we find EOB parameters $(e_0, \langle\Omega\rangle_0)$, a time-shift δt, and an overall amplitude offset C to minimise

$$\int_{t_{\text{junk}}}^{t_{\text{max}}} \left| A_{22}^{\text{NR}}(t) - A_{22}^{\text{EOB}}(t + \delta t; e_0, \ell_\pm, \langle\Omega\rangle_0) + C \right| \, \mathrm{d}t. \tag{7}$$

The time-shift δt aligns the time-axes of the EOB evolution with the NR evolution (e.g. to account for finite-radius GW extraction effects) and the overall offset C is likewise necessary to reach good agreement and a robust fit in the light of using a finite-radius NR waveform. In addition, for systems with low eccentricities, the EOB relativistic anomaly is varied over the two choices $\ell_\pm = \{0, \pi\}$ to account for rare cases that the NR simulation switches into a periastron-configuration, rather than the intended apastron-configuration (a more detailed explanation is provided below). Figure 2 also plots this best-fit EOB waveform.

(vii) From the best-fit EOB waveform, obtain a predicted time to merger $T_{\text{merger}}^{\text{fit}}$ and initial eccentricity e_0^{fit}. If e_0^{fit} and $T_{\text{merger}}^{\text{fit}}$ are sufficiently close to our target eccentricity e_0^{target}

---

[8] The relativistic anomaly ζ employed in the SEOBNRv5EHM model represents a different radial phase parameter than the mean anomaly ℓ. While the evolution of these parameters varies across radial orbits, they are defined such that both satisfy $\zeta = \ell = 0$ at periastron and $\zeta = \ell = \pi$ at apastron.
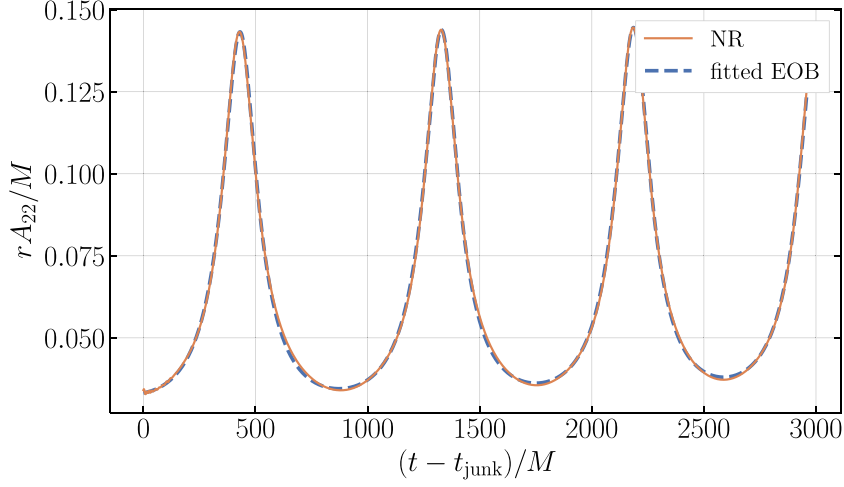
Figure 2. Waveform-based eccentricity control. Shown is a single step of eccentricity control, where the blue curve corresponds to A_{22} obtained via finite-radius extraction in an NR simulation, and the dashed orange curve corresponds to the best-fit `SEOBNRv5EHM` waveform. t_{junk} corresponds to the time at which junk has decreased by an acceptable amount for us to start fitting, which typically takes $\sim 100M$. System corresponds to a particular eccentricity control iteration for the tenth entry in table 2.

and time to merger $T_{\text{merger}}^{\text{target}}$ (within $\pm 10^{-4}$ and $\pm 50M$ respectively), and $\ell_{\pm} = \pi$, then the eccentricity control procedure was successful. Exit the iterative loop and continue the NR simulation.

(viii) Extract the initial EOB dynamical parameters $\left(r_0^{\text{fit}}, \omega_0^{\text{fit}}, p_r^{\text{fit}}\right)$ from the EOB fit obtained in step (vi). Update the NR initial data parameters based on differences between these current EOB parameters and the target EOB parameters determined in step (ii) above:

$$D_0 \leftarrow D_0 \frac{r_0}{r_0^{\text{fit}}}, \tag{8}$$

$$\Omega_0 \leftarrow \Omega_0 \frac{\omega_0}{\omega_0^{\text{fit}}}, \tag{9}$$

$$\dot{a}_0 \leftarrow \dot{a}_0 \frac{p_r}{p_r^{\text{fit}}} \frac{r_0^{\text{fit}}}{r_0}. \tag{10}$$

(ix) Go to step (iv).

For large eccentricities, the inclusion of the fitted parameter $\ell_{\pm}$ is not required, as the behaviour of the binary at periastron and at apastron is quite distinct. However, for eccentricities $e \lesssim 10^{-2}$, the motion of the BHs is dominated by the monotonic inspiral as opposed to the eccentricity-driven oscillations. As such, it can happen that between eccentricity iterations, the NR simulation switches from starting at apastron to starting at periastron. The same is true for the constant offset C: when the waveform is dominated by large, eccentricity-driven oscillations (e.g. as in figure 2), the inclusion of C in the fit makes little difference. However, for lower eccentricities, the near-zone effects become more noticeable and may degrade the quality of the fit.

Table 1. Test cases for waveform-based eccentricity control procedure. The last column lists the actual time to merger obtained by the target NR simulation.

	q	$\vec{\chi}_1$	$\vec{\chi}_2$	e_0^{target}	$T_{\text{merger}}^{\text{target}}$	T_{merger}
Case 1	1	$(0,0,0)$	$(0,0,0)$	0.123	$11\,543M$	$11\,505M$
Case 2	2	$(0,0,0.8)$	$(0,0,0.8)$	0.496	$11\,688M$	$11\,468M$
Case 3	1	$(0.7,0,0.4)$	$(0.8,0,0)$	0.395	$14\,522M$	$13\,935M$
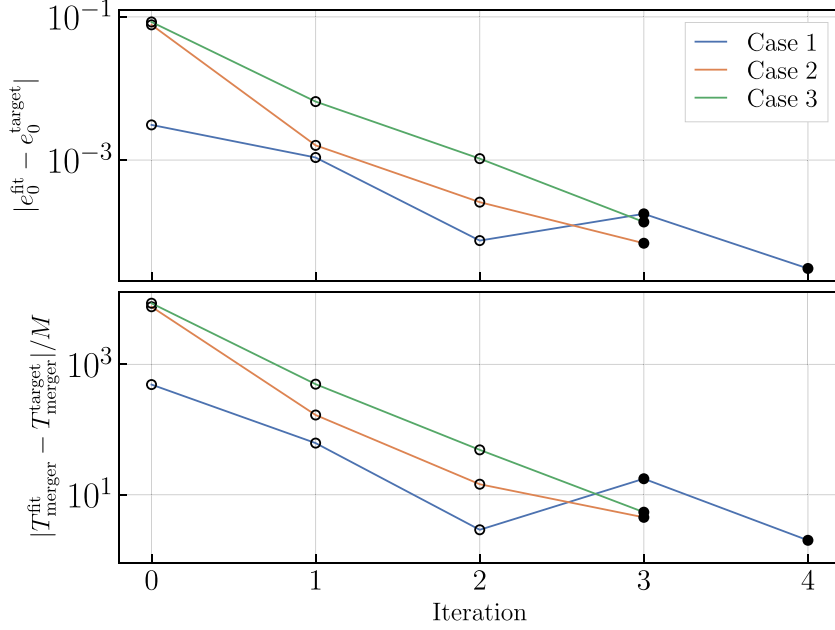
Figure 3. Performance of our eccentricity control procedure. Plotted is the convergence of $(e_0^{\text{fit}}, T_{\text{merger}}^{\text{fit}})$ for test cases defined in table 1. Open circles indicate iterations performed at low resolution to save computational time, while solid circles indicate iterations performed at production-level resolutions. Note that $T_{\text{merger}}^{\text{fit}}$ is the estimated time to merger predicted by the best fit SEOBNRv5EHM system, not the actual time to merger.

Let us now investigate the efficacy of the iterative procedure just defined. We pick three representative cases, defined in table 1. Specifically, we include a non-spinning system, an aligned spin system, as well as a precessing configuration.

Figure 3 shows the convergence of this iterative procedure for our test-configurations. For improved computational efficiency, we perform the first few iterations of eccentricity control at a numerical resolution lower than that we intend to use for our final simulation (referred to as 'rough eccentricity control', and indicated by open circles in figure 3). The final iterations (filled circles) are run at production resolutions. NR simulations at different numerical resolution will, in general, result in slightly different eccentricity. As such, the switch from low to high resolution can move us away from our target $(e_0^{\text{target}}, T_{\text{merger}}^{\text{target}})$, as can be seen in the blue curve. We find that the number of iterations required seems largely independent of the parameters of the BBH, usually taking 3 or 4 iterations.

We emphasise that the convergence plotted is that of the *expected* time to merger $T_{\text{merger}}^{\text{fit}}$, calculated from the EOB model. This will, in general, differ from the merger time of the NR

evolution by a few $100M$; see the last column in table 1. There are several possible reasons for the discrepancy between T_{merger} and $T_{\text{merger}}^{\text{fit}}$; while it is possible this arises due to inaccuracies of the EOB model in parts of the parameter space, the results of Gamboa *et al* [38] indicate this is unlikely to be the dominant source of these errors. More likely is the fact that during step (vi), we are comparing an un-extrapolated, finite radius NR waveform with an EOB waveform associated with future null infinity. In any case, our procedure satisfies two important requirements: First, the achieved T_{merger} is close enough to $T_{\text{merger}}^{\text{target}}$ for practical applications: Neither do the resulting NR simulations waste large amounts of CPU time simulating unneeded earlier parts of the inspiral, nor are the simulations accidentally much shorter than desired. Secondly, $T_{\text{merger}}^{\text{target}}$ and T_{merger} correlate very well: If we change $T_{\text{merger}}^{\text{target}}$ by a small fraction of an orbital period (say, $20M$), then the actual T_{merger} changes by a closely matching amount. This property is essential in constructing sequences of simulations with nearly uniform spacing in mean anomaly.

In addition to the runs shown in figure 3, we have also tested the procedure further for spin-aligned systems with mass-ratios up to $q = 6$, BH spins up to $\chi_i = 0.8$, and eccentricities $10^{-3} \leqslant e_0 \leqslant 0.5$. For such eccentricities, we can achieve control over the target eccentricity e_0^{target} to better than 10^{-4}. To extend this method to lower eccentricities (as well as to obtain more accurate control over the time to merger) will likely require switching from using finite-radius waveforms, to using extrapolated waveforms (either via partial extrapolation, or Cauchy Characteristic Extraction).

Finally, we have performed preliminary tests for precessing systems, an example of which is the green curve in figure 3. While SEOBNRv5EHM contains no precession effects, we expect that 1) early in inspiral, for a short amount of orbits the precession effects are negligible, and 2) the time to merger from a given orbit is dominated by eccentricity dependence as opposed to non-aligned spin component dependence. Since there is currently not an agreed-upon way of defining eccentricity from the gravitational waveform for precessing systems, it is difficult to provide an estimate of the precision of our eccentricity control. We find that for precessing systems we can control e_0^{fit} to be within $\pm 10^{-3}$ of e_0^{target} for eccentricities ~ 0.5, while for a target $T_{\text{merger}}^{\text{target}}$ of approximately $12\,000M$ we can control the time to merger to within $\pm 500M$.

3. Results

3.1. Two-dimensional parameter survey in (e, ℓ)

To isolate the impact of both eccentricity and mean anomaly, we must ensure that we are covering the entire two-dimensional (e, ℓ) parameter space in a controlled way. Previous works [49, 81] generate one-parameter sequences of simulations with increasing eccentricity, with little control over mean anomaly or relied on randomness to generate simulations with different mean anomaly [36].

To ensure proper attention is given to both eccentricity parameters, we seek to generate sequences of simulations with *equal eccentricity*, but with uniform coverage over reference mean anomaly. To do so, we will use the eccentricity control method developed in section 2 to construct a sequence of 13 simulations such that $T_{\text{merger}}^{\text{target}}$ changes by one orbital period during the sequence, and such that e_0^{target} changes slightly, to keep eccentricity at a reference epoch constant. Because all our simulations start at apastron, the variation of $T_{\text{merger}}^{\text{target}}$ through one radial period causes mean anomaly at the reference point to cycle through a full $[0, 2\pi]$ interval. The exact values are found via root-finding on EOB initial parameters, such that the EOB waveform at the reference epoch has the desired constant eccentricity and varying mean

Table 2. e_0^{target} and $T_{\text{merger}}^{\text{target}}$ used for the mean anomaly sequence presented in figure 4. Bold faced entries represent the three coloured simulations presented throughout the paper.

e_0^{target}	0.5000	**0.5000**	0.4984	0.4974	0.4964	**0.4948**	0.4937
$T_{\text{merger}}^{\text{target}}$	$11\,915M$	**$11\,884M$**	$11\,798M$	$11\,719M$	$11\,642M$	**$11\,557M$**	$11\,478M$
e_0^{target}	0.4925	0.4912	**0.4899**	0.4886	0.4877	0.4877	
$T_{\text{merger}}^{\text{target}}$	$11\,398M$	$11\,318M$	**$11\,238M$**	$11\,158M$	$11\,084M$	$11\,021M$	
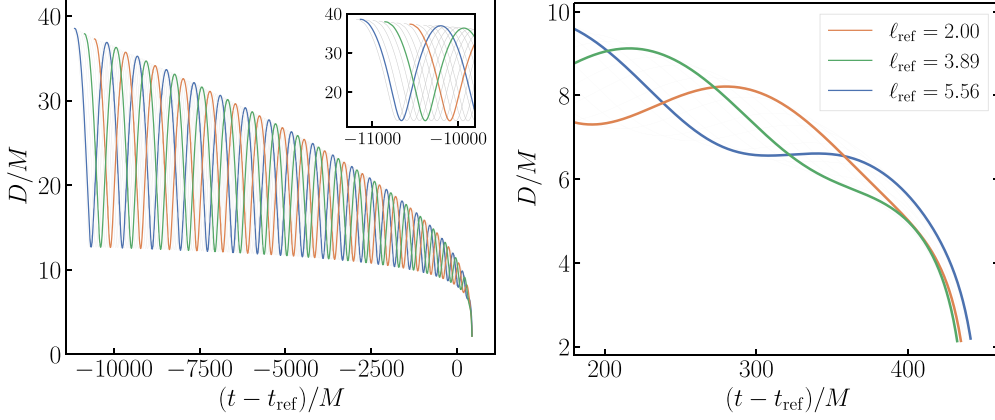
Figure 4. Sample sequence of 13 NR simulations spanning mean anomaly. Each curve corresponds to a full NR simulation with $q = 1$ and $\chi_i = 0$, where the initial conditions were generated using our new eccentricity control method. The common envelope showcases the control obtained over *both* eccentricity and mean anomaly. Three simulations are highlighted in colour.

anomaly. The results, listed in table 2, are then used in the eccentricity tuning procedure of section 2. We will then generate 3 more of these sequences with 12 simulations each for varying values of orbital eccentricity, allowing us to probe the impact of eccentricity itself.

Figure 4 showcases a sample sequence of 13 simulations of constant eccentricity. Plotted is the coordinate separation of the BHs throughout the simulation, with the time-axis aligned at orbit-averaged frequency $\langle \omega_{22} \rangle = 0.069/M$. We see that all simulations in figure 4 share the same envelope of maxima/minima of separation. While we provide no proof, it is expected that for most sensible evolution gauges, sequences of equal eccentricity should share a common envelope of their respective separation curves. We quantify how constant the eccentricity is within the sequence in the appendix. The right panel of figure 4 zooms in on the transition-to-plunge portion of the simulation. Depending on the specific reference mean anomaly, both the length and shape of the final orbit can be markedly altered. This highlights that the type of 'merger geometry' obtained will depend on the specific mean anomaly of each system.

Figure 5 plots the amplitude of the (2,2) mode A_{22} for each of the simulations in table 2, aligned by the time at which the orbit-averaged frequency is $\langle \omega_{22} \rangle = 0.069/M$. The inset shows a zoom-in on the merger portion of the waveform. Again, the shared envelope formed by the local maxima of A_{22} demonstrates the constant reference eccentricity throughout the sequence. We observe that both the amplitude of the peak of the $(2, 2)$ mode, as well as the time taken from t_{ref} to the peak show a cyclic dependence on the reference mean anomaly.
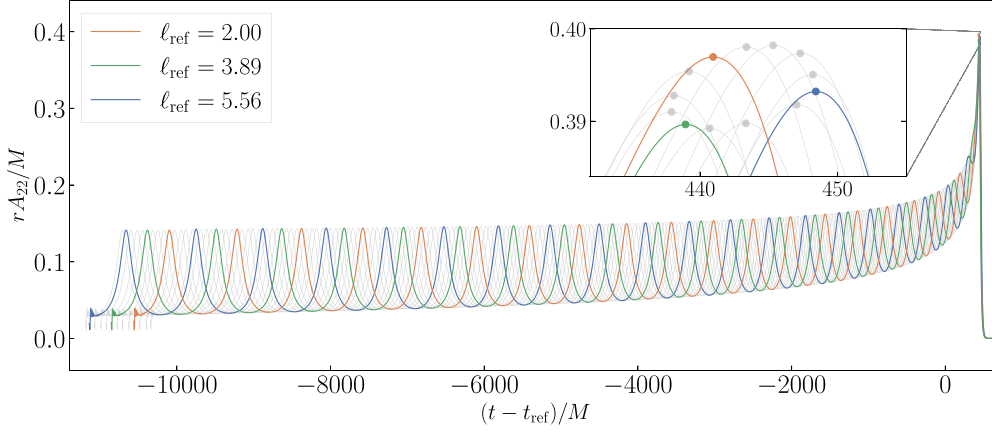
Figure 5. GW amplitude for the mean anomaly sequence with $e_{\text{ref}} = 0.17$. Shown is A_{22} for the NR simulations arising from table 2. Variations of mean anomaly across this sequence manifest themselves as 'sliding' of the extrema during the inspiral, and as modulations of amplitude and time of $\max(rA_{22}/M)$, as indicated by the circles in the inset.

Let us now explore the dependence on mean anomaly within this sequence of simulations in more detail, continuing to use a reference frequency $\langle\omega_{22}\rangle = 0.069/M$ for reporting mean anomaly and eccentricity. Specifically, we consider the maximum of the amplitude of the $(2, 2)$ GW-mode $(\max(rA_{22}/M))$, the peak GW luminosity (L) and the remnant mass and remnant spin $(M_f$ and $\chi_f)$. Figure 6 plots these four quantities as a function of the reference mean anomaly.

We see that the dependence of each of these quantities on mean anomaly is oscillatory, with the largest deviations (in L) having relative magnitudes of $\sim 5\%$. The horizontal dashed lines in each panel represent the corresponding value for quasi-circular inspirals, demonstrating that eccentricity can lead to either an increase or decrease in merger quantities depending on the specific value of mean anomaly obtained.

Given our parametrisation, we expect the BH systems to be 2π-periodic in mean anomaly, and to vary smoothly with respect to mean anomaly. As such, we can expand the dependence of any particular quantity in terms of a Fourier series in mean anomaly. The fact that the oscillations are (nearly) about the quasi-circular value indicates that this is the dominant contribution to the constant term in the expansion, and figure 6 indicates that the first mode of the Fourier series dominates the oscillatory behaviour. We expand the data plotted in figure 6 in a series of the form

$$\delta X \equiv X - X_{\text{QC}} = A_0 + \sum_{k=1}^{m} A_k \sin\left(k\ell + \phi_k\right). \tag{11}$$

Here X denotes any of our four quantities of interest, and we subtract off the quasi-circular value so that A_0 directly represents the mean anomaly averaged change in that value due to eccentricity. We keep the first three terms in the expansion, $m = 2$. While we can fit for higher harmonics, we find that our limited dataset makes it difficult to ascertain the accuracy of these fits.
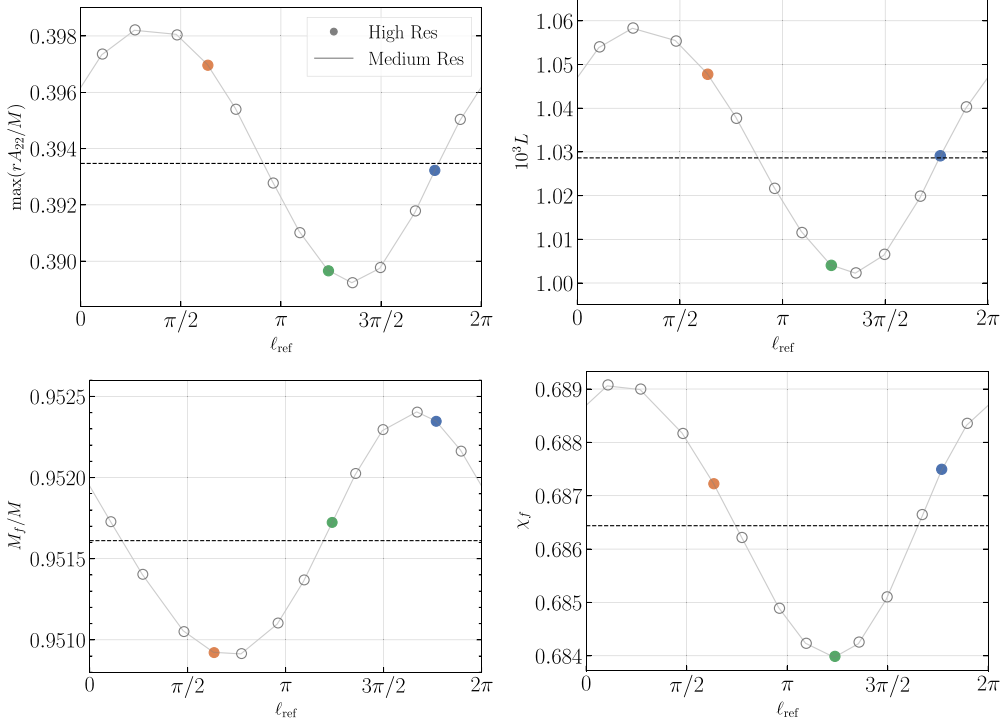
Figure 6. Dependence of merger quantities on mean anomaly. Here, we plot the peak of A_{22}, peak luminosity, and remnant mass and spin for the systems shown in figure 4. Note that each quantity can be both increased and decreased relative to their quasi-circular value (indicated by the horizontal dashed black lines). Coloured points correspond to the highlighted simulations in figure 4. The faint lines in each panel represent results from lower-resolution numerical simulations; they are visually indistinguishable from the high-resolution simulations plotted as symbols, showcasing that numerical truncation error is subdominant.

Figure 7 plots partial sums of the expansions (11), confirming that the constant term is slightly different from the quasi-circular value, and that the first mode dominates the oscillations. The second harmonic is a factor ~10 smaller than the first harmonic, still large enough to be easily visible in figure 7.

Turning towards the dependence on eccentricity, we choose three additional values of reference eccentricity, and perform NR simulations at several values of reference mean anomaly, bringing our set of simulations up to 49 simulations. Figure 8 represents (e, ℓ) for these simulations in a polar plot, highlighting the uniform coverage our technique achieves. The colour-coding of figure 8 conveys information about the peak-amplitude of the $(2, 2)$ GW mode for all the simulations. Specifically, the colour represents the difference between $\max(rA_{22}/M)$ of each eccentric simulation to that of the quasi-circular simulation, normalised by each simulation's eccentricity. Going around the centre of figure 8 at fixed eccentricity, one sees one oscillation of $\delta \max(rA_{22}/M)$, duplicating the oscillatory behaviour of $\max(rA_{22}/M)$ seen in figure 6. Going radially in figure 8, one notices that the colours are nearly constant; this indicates that $\delta \max(rA_{22}/M)$ is proportional to the eccentricity of the simulations.

The data plotted in figures 6 and 8 depends on the reference point chosen to extract eccentricity and mean anomaly. If the reference point moves earlier (farther before merger), then the
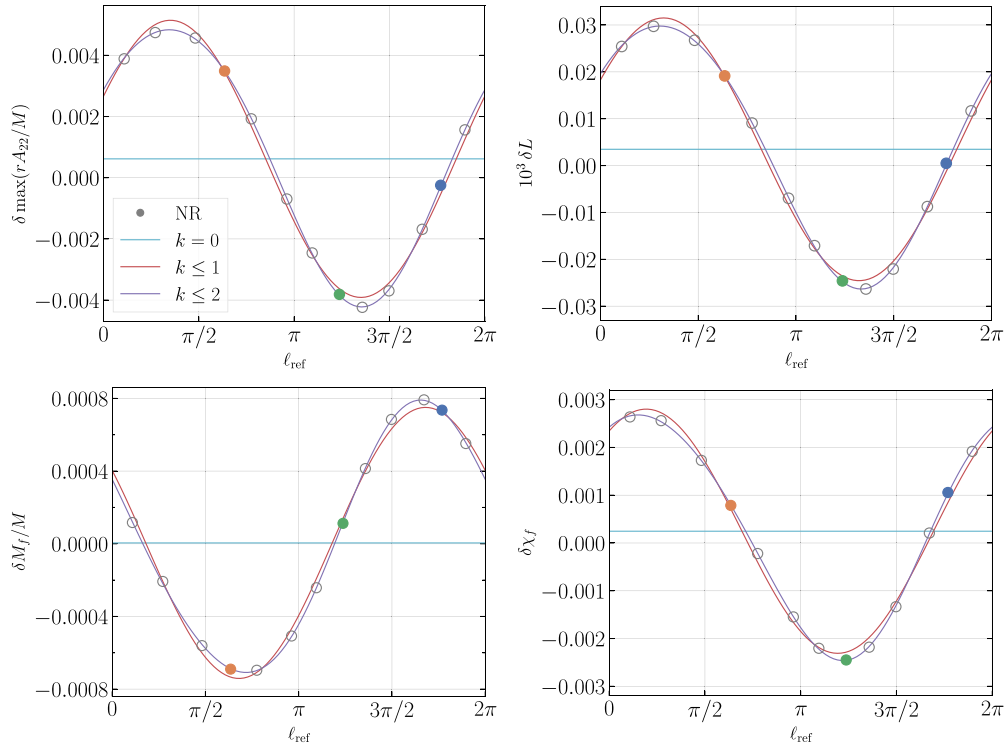
Figure 7. Presence of different harmonics in each quantity. Plotted are partial sums of (11), including only the constant term ($k = 0$), up to first harmonic ($k \leqslant 1$) and up to second harmonic ($k \leqslant 2$).

extracted eccentricities will be larger, owing to the decay of eccentricity during the inspiral. Furthermore, the extracted mean anomalies will cycle once through the interval $[0, 2\pi]$ with each radial oscillation period the reference point moves earlier. Because the inspiral rate of eccentric binaries depends on their eccentricity, the mean anomaly values extracted at earlier times will dephase between simulations with different eccentricities: The very simple overall behaviour seen in figure 8 is only present when ℓ is extracted sufficiently close to merger (in the figure, at $t - t_{\text{peak}} = -700M$). Since it is the merger behaviour that determines $\delta \max(rA_{22}/M)$, it comes at no surprise that its dependence on (e, ℓ) is simplest when a reference point very near merger is chosen.

While figure 8 indicates that the overall scale of the oscillations scales linearly with eccentricity, one might wonder how the individual harmonics presented in figure 7 scale with increasing eccentricity. Focusing on $\delta \max(rA_{22}/M)$, we repeat fits of the form (11) separately for the four different mean anomaly sequences at different eccentricities, and plot the obtained amplitudes in the top panels of figure 9. Figure 7 indicates that the dominant contribution to (11) is the first harmonic A_1, which we find indeed scales almost linearly.

To understand the phenomenology of these scalings, first note that the amplitudes of (11) can be extended to depend on eccentricity using a low eccentricity expansion:

$$A_k(e) = a_1 e + a_2 e^2 + a_3 e^3 + a_4 e^4 + \dots \tag{12}$$
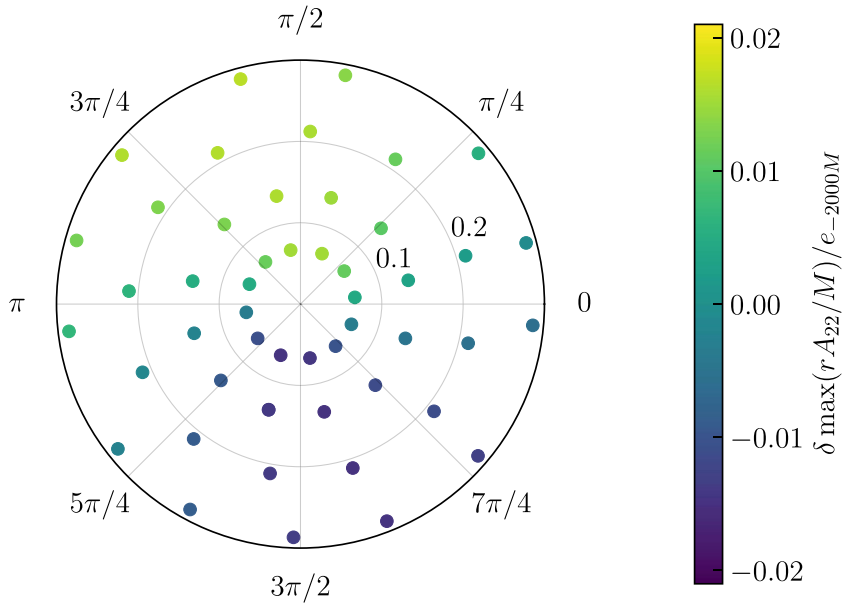
Figure 8. Deviation of $\max(rA_{22}/M)$ across eccentricities. Plotted are 4 sequences of NR simulations of varying eccentricity (indicated by constant radius rings), with eccentricities $e_{-2000M} = 0.095, 0.185, 0.272, 0.346$. The angle of each point corresponds to ℓ_{-700M}, while distance from the origin is equal to e_{-2000M}. Each point is coloured by the deviation of the peak of A_{22} divided by e_{-2000M}, to highlight that the range of $\delta \max(rA_{22}/M)$ grows approximately linearly in e (as each ring spans the same $\delta \max(rA_{22}/M)/e_{-2000M}$ range).

Because we are expanding the difference to the quasi-circular limit, the constant a_0 term vanishes. Consider a system characterised by a reference (e, ℓ). Under the inter-change of the definition of periastron and apastron, we observe that the same physical system would instead be characterised by $(-e, \ell + \pi)$. As such, any eccentric correction should be invariant under this re-definition. This limits the number of possible terms in the eccentric expansion of A_k, as these terms come with a factor of $\sin(k\ell)$. Specifically, keeping only the first two terms in the expansion, for even k we should expect the dependence on e to be

$$A_k = a_2 e^2 + a_4 e^4, \tag{13}$$

while for odd k, we obtain

$$A_k = a_1 e + a_3 e^3. \tag{14}$$

The dashed curves in figure 9 show fits of (13) and (14) as appropriate. We find that these fits match the data well, approaching the truncation error of our data. However, a more careful consideration of these fits (including the exploration of higher-order contributions) will be required to build fits of these deviations across parameter space.
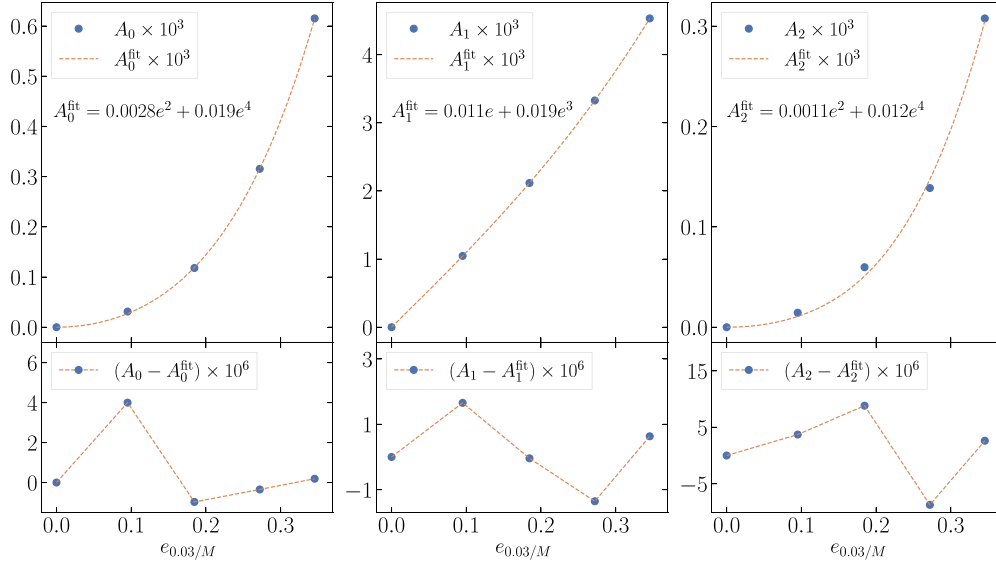
Figure 9. Scaling of mean anomaly harmonic amplitudes with eccentricity. We perform the analysis of figure 7 for each of the constant eccentricity sequences shown in figure 8. Plotted are the amplitudes A_i of the expansion of peak GW amplitude A_{22} in the form of (11). The dashed lines correspond to fits of (13) and (14) as appropriate. We include an additional data point for $e_{0.03/M} = 0$, as we know the correction to the quasi-circular value must vanish. The lower panel shows the residuals of the fits.

3.2. Interpreting one-parameter eccentric sequences

With our comprehensive NR data-set in hand, and the accompanying understanding of eccentric binaries, we can now discuss the phenomenology observed in other eccentric explorations. Several other works have reported a seemingly oscillatory dependence of merger-related quantities (e.g. maximum waveform strain $\max(rA_{22}/M)$) on eccentricity [51–53, 81, 82]. In contrast, figure 9 indicates a monotonic dependence on eccentricity. Our claim is that such reported oscillations arise from taking a *one-parameter* sequence of simulations across the two-dimensional (e, ℓ) parameter space. As e changes along such a one-parameter sequence, typically ℓ will also change in some way, related to the precise description being used to construct the one-parameter sequence. It is then the dependence on ℓ (as exhibited in figure 6) that induces a seemingly 'oscillatory behaviour with eccentricity'.

To support our claim, we generate a one-dimensional sequence of eccentric BBH simulations following the procedure of Healy and Lousto [49]: we fix the intrinsic BH parameters to be non-spinning, equal mass throughout this calculation, and begin with $(D_0, \Omega_0, \dot{a}_0)$ such that the BHs are in a quasi-circular configuration. We choose a large initial separation of $D_0 \approx 24.1M$, corresponding to a quasi-circular inspiral of duration $30\,000M$, in order to always have a sufficiently long inspiral to measure eccentricity and mean anomaly with `gw_eccentricity`. This furthermore will allow us to exhibit a large number of oscillations of $\max(rA_{22}/M)$ as we proceed through this sequence. We then generate a sequence of simulations where we keep D_0 and $\dot{a}_0$ unchanged, but decrease Ω_0, resulting in simulations with increasing initial eccentricity and decreasing time to merger. For each simulation, we estimate eccentricity at a reference time $2000M$ before merger, and we record the maximum amplitude of the (2, 2) mode of the emitted gravitational radiation, $\max(rA_{22}/M)$. Results from 31 NR
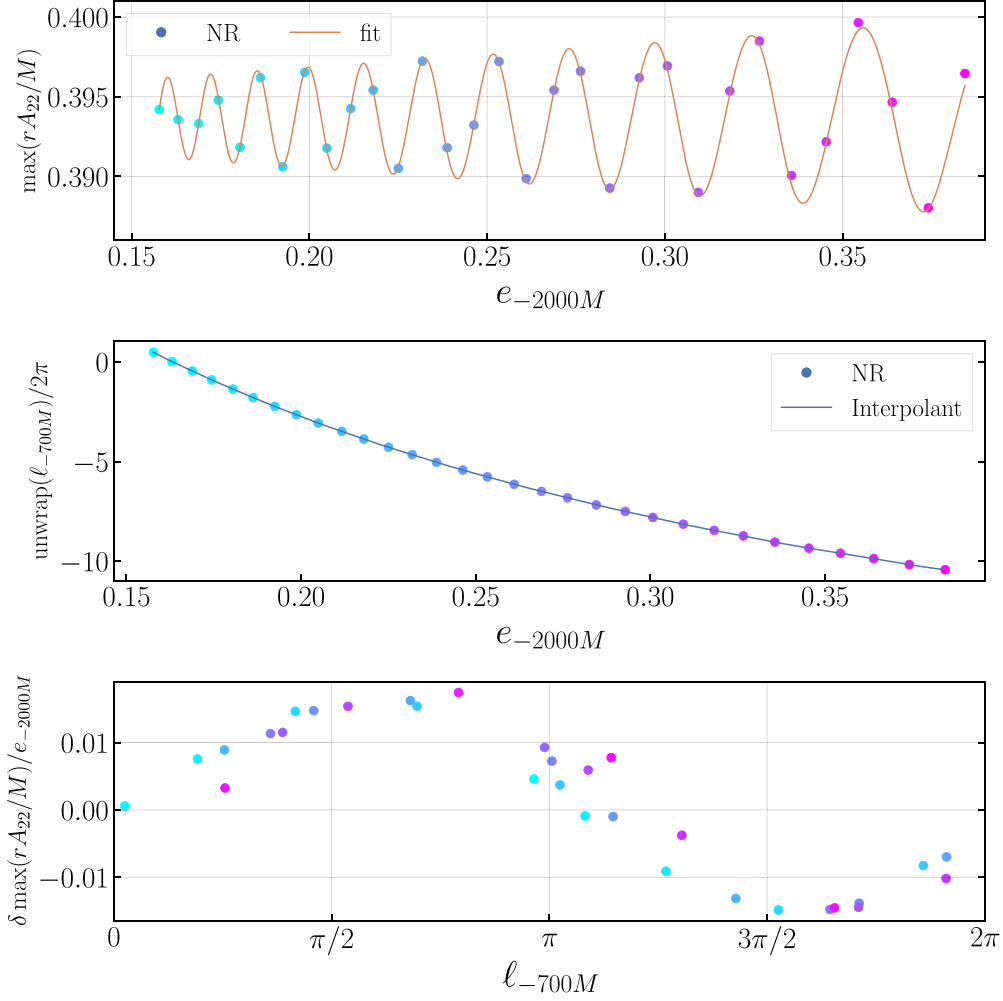
Figure 10. Typical sequence obtained if mean anomaly is neglected. Sequence consists of simulations where the initial separation and in-going velocity of the BHs is fixed, but the initial orbital frequency Ω_0 is slowly decreased. Top: peak of A_{22} for the sequence. The orange line corresponds to the model (15). Middle: unwrapped reference mean anomaly as a function of the reference eccentricity. Bottom: deviation of the peak of rA_{22}/M as a function of the mean anomaly. Colouring corresponds to e_{-2000M}.

simulations are plotted as filled circles in the top panel of figure 10. This plot of $\max(rA_{22}/M)$ vs e_{-2000M} indeed appears to exhibit oscillatory behaviour with eccentricity. However, the simulations of this sequence will also have different mean anomaly at a fixed reference epoch, here chosen as $700M$ before merger. In fact, each time the number of radial periods of the inspiral decreases by one, we should approximately cycle through a full period of reference mean anomaly near merger. The mean anomaly of each of the 31 simulations is plotted in the middle panel of figure 10, made continuous by suitable additions of 2π, and divided by 2π, so that the *y*-axis represents the difference in number of radial periods each simulation completes, relative to the simulation with the smallest eccentricity.

To interpret the NR data shown in figure 10, we utilise the functional form for the peak amplitude that we derived in section 3.1, namely

$$\max\left(rA_{22}/M\right)\left(e_{-2000M}, \ell_{-700M}\right) = \max\left(rA_{22}/M\right)^{\text{QC}} + e_{-2000M}A_1\sin\left(\ell_{-700M} + \ell_0\right), \quad (15)$$

where for simplicity we have elected to keep only the first harmonic in mean anomaly (as well as the first term in the eccentricity expansion), and exclude the constant offset. Here ℓ_0 represents the offset in mean anomaly at reference epoch to the phasing of the merger amplitude $\max(rA_{22}/M)$. The one-parameter sequence of simulations covers a wide range of eccentricities, with correspondingly somewhat different inspiral rates; therefore, ℓ_0 will mildly depend on eccentricity, even for our reference epoch $t = -700M$ close to merger[9]. Because the variations in ℓ_0 are mild, we approximate it as a first order Taylor expansion,

$$\ell_0\left(e_{-2000M}\right) = B_0 + B_1 e_{-2000M}. \quad (16)$$

Our NR simulations give us 31 data-points for $\max A_{22}$ in the *two*-dimensional (e, ℓ) plane, and (15) with (16) represents the expected behaviour of this quantity, given the three parameters A_1, B_0, B_1. We now fit these three unknown parameters to the NR data, and thus achieve the full functional form $\max(rA_{22}/M)(e, \ell)$. The result of this fit is plotted as a solid curve in the top panel of figure 10, where we evaluate $\ell_{-700M}(e_{-2000M})$ for arbitrary e_{-2000M} via the interpolant shown in blue in the middle panel. The three-parameter fit reproduces all variations in the data-points, exhibiting that indeed within the eccentricity range considered in figure 10, the one-dimensional sequence of simulations proceeds through 10 maxima and minima of $\max(rA_{22}/M)$, corresponding to 10 cycles through mean anomaly. Finally, the bottom panel of figure 10 plots the deviations of $\max(rA_{22}/M)$ from the quasi-circular value as a function of mean anomaly. After normalisation by eccentricity, the data approximately collapses to a single sinusoidal curve, reminiscent of figure 6.

Compared to other works [51–53], our dataset seemingly contains many more oscillations. This arises from the length of our simulations: as previously stated, each time the number of radial periods decreases by one, the mean anomaly defined near merger will cycle through 2π. One conclusion is that even for significant eccentricities near merger, one can approximate the behaviour of several quantities in the two-dimensional (e, ℓ) space with simple formulae (requiring only 3 parameters fit from data).

3.3. EOB estimates of the final mass and spin

While several of our results may only be accessible via full NR simulations, there are hints that others, such as the final mass and spin of the remnant BH, may be well approximated using semi-analytical methods. The idea of analytically estimating the final mass and spin of a BBH coalescence was introduced in [83, 84]. In this work, the final mass and spin were estimated from the EOB Hamiltonian H_{EOB} and orbital angular momentum p_ϕ at the end of the plunge, providing a prediction of such quantities for a remnant generated by a BBH merger. With the breakthrough of NR [85–87], the picture outlined in [83] was shown to be qualitatively, and to some extent quantitatively, correct [88]. The main physical ingredient which is lacking in these early estimates is the loss of energy and angular momentum during the ringdown phase.

---

[9] Here, as in figure 8, we choose to define eccentricity and mean anomaly at different times to merger. Currently, `gw_eccentricity` produces oscillatory eccentricities very close to merger, likely due to the spline interpolation. To avoid this, we define our reference eccentricity earlier in the inspiral.

Later works [89, 90] refined the accuracy of EOB estimates by approximately accounting for such losses, as

$$M_f = H_{\text{EOB}}\left(t_{\text{match}}\right) - E_{\text{ringdown}}, \tag{17}$$

$$J_f = J_{\text{EOB}}\left(t_{\text{match}}\right) - J_{\text{ringdown}}. \tag{18}$$

Here, t_{match} represents the time at which the inspiral-plunge and ringdown waveforms are connected, around the peak of the EOB orbital frequency. The energy and angular momentum losses during the ringdown, E_{ringdown} and J_{ringdown}, were approximated by a suitable rescaling of test-particle results [91]. Recent EOB models compute these quantities from more accurate NR fits for binaries on quasi-circular orbits [92, 93]. While analogous fits have started to become available for eccentric BBHs [82], the limited number of NR simulations covering the eccentric parameter space prevents a precise assessment of their accuracy, particularly when spin effects are also included.

Here, we present an approximate method which offers a practical approach to account for merger effects in current EOB models for eccentric BBHs, relying only on quasi-circular NR fits. Focusing on the final mass, let us consider (17) for an eccentric and a quasi-circular BBH with the same component masses and spins,

$$M_f^{\text{ecc}} = H_{\text{EOB}}\left(t_{\text{match}}^{\text{ecc}}\right) - E_{\text{ringdown}}^{\text{ecc}}, \tag{19}$$

$$M_f^{\text{QC}} = H_{\text{EOB}}\left(t_{\text{match}}^{\text{QC}}\right) - E_{\text{ringdown}}^{\text{QC}}. \tag{20}$$

Since the binary circularises during the inspiral, we assume that the energy emitted during the ringdown stage is similar in the two cases,

$$E_{\text{ringdown}}^{\text{ecc}} \simeq E_{\text{ringdown}}^{\text{QC}}. \tag{21}$$

We can then approximate the final mass for an eccentric BBH as

$$M_f^{\text{ecc}} \simeq M_f^{\text{QC}} + \left[H_{\text{EOB}}\left(t_{\text{match}}^{\text{ecc}}\right) - H_{\text{EOB}}\left(t_{\text{match}}^{\text{QC}}\right) \right]. \tag{22}$$

In this equation, the M_f^{QC} value can be obtained from NR fits for quasi-circular BBH mergers, or—for the present study of equal-mass, non-spinning BBH—it can be directly read off from NR simulations [61]. The second term can be estimated using the `SEOBNRv5EHM` eccentric waveform model [38]. In this model, the value of $t_{\text{match}}^{\text{QC}}$ is calibrated to quasi-circular BBH NR simulations, while $t_{\text{match}}^{\text{ecc}}$ is not calibrated to eccentric NR simulations. However, the predicted attachment time $t_{\text{match}}^{\text{ecc}}$ employs indirectly the calibration to quasi-circular NR simulations from the `SEOBNRv5HM` model [18], hence making (22) a reasonable approximation[10].

Analogously, the final spin of an eccentric BBH merger can be estimated via

$$J_f^{\text{ecc}} \simeq J_f^{\text{QC}} + \left[p_\phi\left(t_{\text{match}}^{\text{ecc}}\right) - p_\phi\left(t_{\text{match}}^{\text{QC}}\right) \right],$$

$$\chi_f^{\text{ecc}} = J_f^{\text{ecc}} / \left(M_f^{\text{ecc}}\right)^2, \tag{23}$$

where J_f^{QC} can also be obtained from NR fits for quasi-circular BBHs. In the rest of this section, we use the `NRSur7dq3Remnant` fits [21] for M_f^{QC} and J_f^{QC}.

---

[10] A similar argument was applied in [94] to estimate corrections for the final mass and spin in Einstein-scalar-Gauss–Bonnet gravity relative to their value in General Relativity.
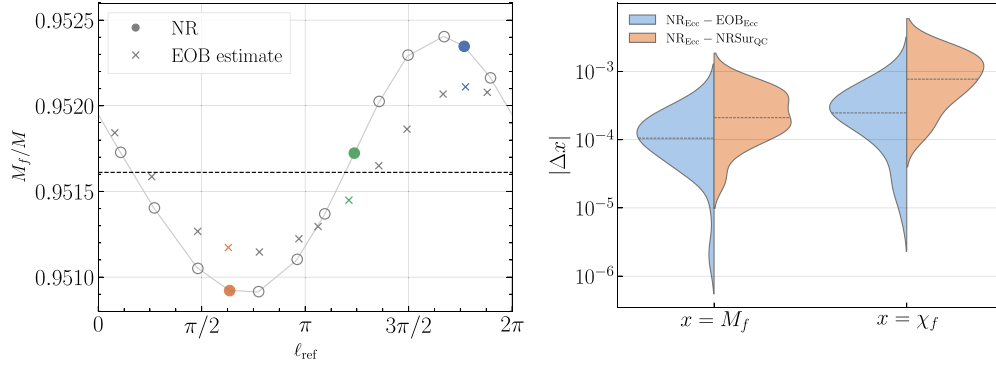
Figure 11. EOB estimates of the final mass and spin. Left: result of (22) plotted with the actual NR data already shown in figure 6. Right: absolute value of the difference between the NR and EOB predictions for the remnant mass and spin (in blue) across all NR simulations presented in this work, along with comparisons to the quasi-circular `NRSur7dq3Remnant` fit (in orange). Horizontal dashed lines indicate the median values.

To assess the accuracy of the estimates equations (22) and (23), we need a mapping between eccentric EOB waveforms and the NR results presented in the previous section, which is complicated because many definitions (including the ones employed in many waveform models) of eccentricity are gauge dependent [95–97]. For the purpose of this work, we employ the method described in [38] to find the optimum EOB waveform given an eccentric NR simulation. This method is based on the one presented in [95], and consists of optimising over the EOB input values of eccentricity and orbit-averaged frequency to get the waveform with the lowest $(2,2)$-mode unfaithfulness; in this optimisation, the waveforms are initialised at apastron. Given the high NR-faithfulness of the `SEOBNRv5EHM` model [38], this approach leads to a good agreement between the gauge-invariant values of eccentricity e_{gw} and mean anomaly ℓ_{gw} extracted from the EOB and NR waveforms at the same reference frequency. In this way, for each NR simulation, we calculate the values of M_f^{ecc} and χ_f^{ecc} from equations (22) and (23) using the `SEOBNRv5EHM` model.

The results for a subset of NR simulations with different values of mean anomaly ℓ_{gw}, but equal values of eccentricity $e_{gw} \simeq 0.17$ at a reference frequency $\langle \omega_{22} \rangle = 0.069/M$, are presented in the left panel of figure 11. In this plot, we include the values of the final mass M_f extracted from the NR simulations, and the corresponding `SEOBNRv5EHM` estimates based on (22). For the EOB data points, the values of e_{gw} and ℓ_{gw} are extracted with the `gw_eccentricity` package at $\langle \omega_{22} \rangle$ from the optimum `SEOBNRv5EHM` waveforms. We observe that the oscillatory dependence of M_f around the quasi-circular value is also captured by the EOB estimates, with the amplitude and phasing being reasonably well reproduced.

To better assess the accuracy of the estimates (22) and (23), the right panel of figure 11 shows the absolute difference between the NR and EOB predictions for the remnant mass and spin (in blue) across all NR simulations presented in this work, along with comparisons to the quasi-circular `NRSur7dq3Remnant` fit (in orange). Horizontal dashed lines indicate the median values. For this comparison, the EOB estimates use the input parameters corresponding to the optimum waveforms. The quasi-circular NR surrogate for the remnant properties does not capture eccentricity-induced variations as those shown in the left panel of figure 11, whereas the EOB estimates reproduce such variations to a reasonable degree. Therefore, the

EOB-estimates reduce differences $|\Delta x|$ in the right panel of figure 11 by a factor ~ 2 for the final mass and ~ 3 for the final spin.

We note that equations (22) and (23) can be evaluated during waveform generation with the `SEOBNRv5EHM` model at negligible computational cost, so that these corrections can be included without requiring additional parameter space fits. It would also be straightforward to produce fits for these corrections using the same techniques applied to NR remnant fits, given the efficiency of generating large numbers of EOB waveforms.

4. Conclusion

In this work, we have presented a complete analysis of eccentric simulations where, for the first time, both eccentric parameters are accounted for. To do so, we propose a new waveform-based eccentricity control method, which we implement in the Spectral Einstein Code `SpEC`. This eccentricity control procedure enables a new, precise control over both reference eccentricity and mean anomaly. We utilise this procedure to generate several sequences of full NR simulations with constant reference eccentricity, but uniform coverage of mean anomaly. We show that, for the parameter space explored, merger-related quantities show an oscillatory dependence on mean anomaly with mean very close to the corresponding quasi-circular value, with the amplitude of these oscillations determined by the eccentricity of the system (see, e.g. figures 6 and 9).

Our results highlight the importance in considering the entire two-dimensional parameter space when studying eccentric systems. Several recent studies have found a seemingly oscillatory dependence of several quantities on eccentricity. By recreating a typical sequence of simulations used in such studies, we demonstrate that the reported oscillations arise from a lack of control over the reference mean anomaly of these systems.

While there are several subtleties in regards to defining reference eccentricity and mean anomaly for a binary, it is shown that so long as one defines these values sufficiently close to merger, the resulting dependence on both eccentricity and mean anomaly is quite simple. This result is promising in the context of waveform modelling, where the inclusion of such effects should be straightforward.

Finally, we show that some of the results in this work may be accessible by analytic models. By considering a previously used phenomenological estimate for the mass of the remnant BH, we show that the `SEOBNRv5EHM` model reproduces oscillations of a similar order of magnitude. This hints at a possible analytic explanation to some of our results, as was also recently explored in [53].

There are many other quantities one can examine using our simulations. Continuing to focus on the merger portion of the evolution, the modification of the mass and spin of the remnant indicate that accounting for both the anomaly and eccentricity is necessary to characterise ringdowns from eccentric systems. Further, the variation of the peak of A_{22} suggests that the excitation coefficients will likely have a similar dependence on both parameters. This is further supported by the notion that, in linear perturbation theory, the excitation coefficients depend on the exact perturbation imparted on the BH [98]. As the mean anomaly picks out the 'merger geometry' obtained, one should expect this will also choose the exact type of perturbation present in the remnant BH. We leave further exploration of these quantities to future works.

It is also interesting to consider the impact of eccentricity and mean anomaly on the recoil kick imparted on the remnant BH due to asymmetric emission of linear momentum [81]. Such

a study, however, comes with some subtle difficulties; for systems of sufficient eccentricity, one obtains non-negligible kicks imparted on the binary system during *inspiral* with each periastron passage. While these kicks are significantly smaller than that imparted on the remnant, their contributions make it more difficult to define the initial rest-frame which we relate the recoil to. As well as this, periastron precession leads to these kicks being imparted in varying directions, which can lead to both constructive and destructive contributions. We leave a more complete exploration of BH recoil to future work.

To account for mean anomaly in modern waveform models, one would have to explore the phenomenology of mean anomaly/eccentricity deviations across more of the parameter space. In particular, one would have to explore the impact of varying the mass-ratio and spins. Preliminary results indicate that the phenomenology of these deviations is similar in other parts of parameter space, indicating that fewer simulations may be required to parametrise these effects. We leave a more complete exploration of the non-precessing parameter space to future work.

While the new eccentricity control procedure presented is sufficient for our purposes, there are several avenues for improvement. Currently, we compare a finite-radius NR waveform to an `SEOBNRv5EHM` waveform associated with future null infinity. Yet more accurate control than what we achieved here may require to extrapolate the NR waveform to future null infinity [99]. One could also attempt to extend the eccentricity control procedure to generic spins, once analytic waveform models with both eccentricity and precessing spins are available.

Data availability statement

The data that support the findings of this study will be openly available following an embargo at the following URL/DOI: https://data.black-holes.org/simulations/index.html [99]. Data will be available from 11 April 2026.

Acknowledgments

Appendix

Table A1 lists the SXS IDs of the simulations analysed in section 3.1. In addition, we provide the initial conditions $(D_0, \Omega_0, \dot{a}_0)$ used to perform these simulations, which were obtained via the eccentricity control procedure described in section 2.2. The values e_0^{target} in table A1 refer to the initial eccentricities reported by the EOB-model utilised in the eccentricity tuning procedure. We extract the actual eccentricities of each NR waveform using `gw_eccentricity` at reference frequency $\langle \omega_{22} \rangle = 0.03/M$, and plot their spread in figure A1. We find that the actual NR eccentricities are constant within each sequence to fractional accuracy of a few 10^{-3}.

Table A2 presents the initial data parameters for the simulations analysed in section 3.2 (this analysis does not utilise eccentricity control).

Table A1. Simulations analysed in section 3.1. The columns show the SXS ID, as well as the initial conditions $(D_0, \Omega_0, \dot{a}_0)$ obtained from the procedure presented in section 2.2.

SXS ID	D_0/M	$M\Omega_0$	$M\dot{a}_0$	e_0^{target}	$T_{\text{merger}}^{\text{target}}/M$
SXS:BBH:4381	38.540	3.032×10^{-3}	2.41×10^{-6}	0.5000	11 915
SXS:BBH:4293	38.527	2.982×10^{-3}	2.07×10^{-6}	0.5000	11 884
SXS:BBH:4304	38.336	3.009×10^{-3}	2.14×10^{-6}	0.4984	11 798
SXS:BBH:4303	38.207	3.027×10^{-3}	2.19×10^{-6}	0.4974	11 719
SXS:BBH:4302	38.072	3.046×10^{-3}	2.23×10^{-6}	0.4964	11 642
SXS:BBH:4301	37.896	3.071×10^{-3}	2.30×10^{-6}	0.4948	11 557
SXS:BBH:4300	37.736	3.094×10^{-3}	2.37×10^{-6}	0.4937	11 478
SXS:BBH:4299	37.590	3.116×10^{-3}	2.44×10^{-6}	0.4925	11 398
SXS:BBH:4298	37.449	3.136×10^{-3}	2.49×10^{-6}	0.4912	11 318
SXS:BBH:4297	37.289	3.160×10^{-3}	2.56×10^{-6}	0.4899	11 238
SXS:BBH:4296	37.137	3.183×10^{-3}	2.63×10^{-6}	0.4886	11 158
SXS:BBH:4295	37.030	3.198×10^{-3}	2.66×10^{-6}	0.4877	11 084
SXS:BBH:4294	36.977	3.205×10^{-3}	2.68×10^{-6}	0.4877	11 021
SXS:BBH:4375	31.321	4.446×10^{-3}	1.95×10^{-5}	0.3748	12 018
SXS:BBH:4374	31.258	4.461×10^{-3}	1.99×10^{-5}	0.3743	11 955
SXS:BBH:4372	31.073	4.507×10^{-3}	2.14×10^{-5}	0.3715	11 822
SXS:BBH:4373	31.068	4.511×10^{-3}	2.19×10^{-5}	0.3705	11 876
SXS:BBH:4371	30.990	4.528×10^{-3}	2.22×10^{-5}	0.3703	11 757
SXS:BBH:4370	30.909	4.548×10^{-3}	2.31×10^{-5}	0.3692	11 692
SXS:BBH:4369	30.832	4.567×10^{-3}	2.39×10^{-5}	0.3680	11 627
SXS:BBH:4380	30.750	4.588×10^{-3}	2.49×10^{-5}	0.3669	11 556
SXS:BBH:4379	30.706	4.598×10^{-3}	2.51×10^{-5}	0.3667	11 491
SXS:BBH:4378	30.622	4.617×10^{-3}	2.54×10^{-5}	0.3665	11 363
SXS:BBH:4377	30.582	4.626×10^{-3}	2.54×10^{-5}	0.3664	11 301
SXS:BBH:4376	30.656	4.610×10^{-3}	2.56×10^{-5}	0.3664	11 425
SXS:BBH:4321	25.721	6.452×10^{-3}	-2.15×10^{-5}	0.2500	11 882
SXS:BBH:4332	25.677	6.470×10^{-3}	-2.17×10^{-5}	0.2496	11 822
SXS:BBH:4331	25.733	6.450×10^{-3}	-2.17×10^{-5}	0.2495	11 940
SXS:BBH:4330	25.629	6.489×10^{-3}	-2.18×10^{-5}	0.2493	11 762

<div align="right">(Continued.)</div>
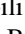
Table A1. (Continued.)

SXS ID	D_0/M	$M\Omega_0$	$M\dot{a}_0$	e_0^{target}	$T_{\text{merger}}^{\text{target}}/M$
SXS:BBH:4329	25.562	6.518×10^{-3}	-2.18×10^{-5}	0.2483	11 700
SXS:BBH:4328	25.512	6.539×10^{-3}	-2.19×10^{-5}	0.2478	11 641
SXS:BBH:4327	25.462	6.559×10^{-3}	-2.19×10^{-5}	0.2472	11 581
SXS:BBH:4326	25.412	6.581×10^{-3}	-2.19×10^{-5}	0.2467	11 522
SXS:BBH:4325	25.362	6.602×10^{-3}	-2.20×10^{-5}	0.2461	11 462
SXS:BBH:4324	25.309	6.624×10^{-3}	-2.20×10^{-5}	0.2455	11 403
SXS:BBH:4323	25.258	6.646×10^{-3}	-2.21×10^{-5}	0.2450	11 344
SXS:BBH:4322	25.210	6.667×10^{-3}	-2.21×10^{-5}	0.2445	11 285
SXS:BBH:4361	22.012	8.639×10^{-3}	-1.79×10^{-5}	0.1248	11 936
SXS:BBH:4360	21.979	8.660×10^{-3}	-1.80×10^{-5}	0.1245	11 881
SXS:BBH:4359	21.948	8.678×10^{-3}	-1.81×10^{-5}	0.1243	11 826
SXS:BBH:4358	21.916	8.698×10^{-3}	-1.81×10^{-5}	0.1241	11 771
SXS:BBH:4357	21.884	8.717×10^{-3}	-1.82×10^{-5}	0.1239	11 716
SXS:BBH:4368	21.851	8.738×10^{-3}	-1.83×10^{-5}	0.1236	11 658
SXS:BBH:4367	21.820	8.756×10^{-3}	-1.84×10^{-5}	0.1234	11 601
SXS:BBH:4366	21.787	8.777×10^{-3}	-1.85×10^{-5}	0.1232	11 543
SXS:BBH:4365	21.754	8.797×10^{-3}	-1.86×10^{-5}	0.1229	11 486
SXS:BBH:4364	21.721	8.818×10^{-3}	-1.87×10^{-5}	0.1227	11 429
SXS:BBH:4363	21.690	8.837×10^{-3}	-1.87×10^{-5}	0.1225	11 374
SXS:BBH:4362	21.662	8.853×10^{-3}	-1.88×10^{-5}	0.1225	11 319
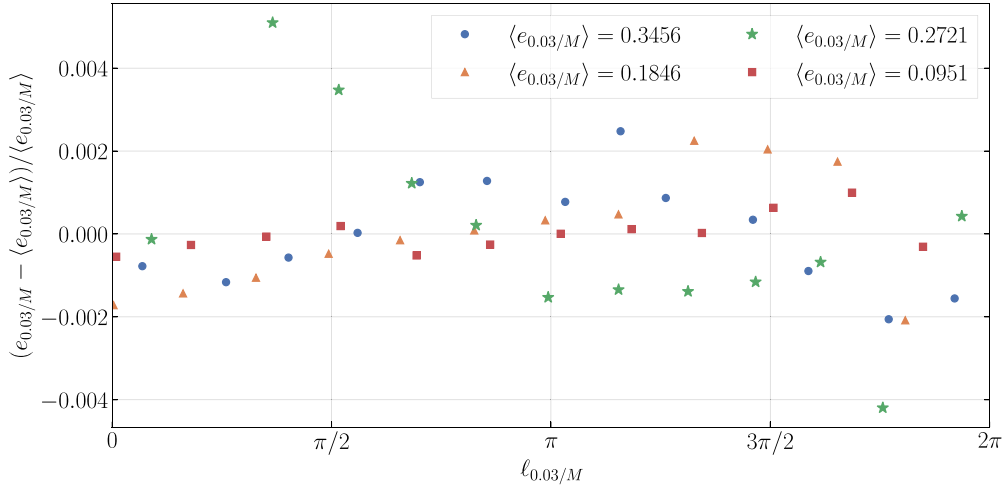
Figure A1. Deviation of eccentricity within each constant-eccentricity sequence. Each colour corresponds to one of the constant eccentricity sequences presented in figure 8. $\langle e_{0.03/M} \rangle$ is computed by taking the average of $e_{0.03/M}$ across each sequence.

Table A2. Simulations analysed in section 3.2. The columns show the SXS ID, as well as the initial conditions $(D_0, \Omega_0, \dot{a}_0)$ used to perform these simulations.

SXS ID	D_0/M	$M\Omega_0$	$M\dot{a}_0$
SXS:BBH:4392	24.102	7.203×10^{-3}	1.02×10^{-5}
SXS:BBH:4408	24.102	7.181×10^{-3}	1.02×10^{-5}
SXS:BBH:4398	24.102	7.158×10^{-3}	1.02×10^{-5}
SXS:BBH:4409	24.102	7.136×10^{-3}	1.02×10^{-5}
SXS:BBH:4399	24.102	7.114×10^{-3}	1.02×10^{-5}
SXS:BBH:4410	24.102	7.092×10^{-3}	1.02×10^{-5}
SXS:BBH:4393	24.102	7.069×10^{-3}	1.02×10^{-5}
SXS:BBH:4411	24.102	7.047×10^{-3}	1.02×10^{-5}
SXS:BBH:4400	24.102	7.025×10^{-3}	1.02×10^{-5}
SXS:BBH:4412	24.102	7.002×10^{-3}	1.02×10^{-5}
SXS:BBH:4401	24.102	6.980×10^{-3}	1.02×10^{-5}
SXS:BBH:4413	24.102	6.958×10^{-3}	1.02×10^{-5}
SXS:BBH:4394	24.102	6.936×10^{-3}	1.02×10^{-5}
SXS:BBH:4414	24.102	6.913×10^{-3}	1.02×10^{-5}
SXS:BBH:4402	24.102	6.891×10^{-3}	1.02×10^{-5}
SXS:BBH:4415	24.102	6.869×10^{-3}	1.02×10^{-5}
SXS:BBH:4403	24.102	6.847×10^{-3}	1.02×10^{-5}
SXS:BBH:4416	24.102	6.824×10^{-3}	1.02×10^{-5}
SXS:BBH:4395	24.102	6.802×10^{-3}	1.02×10^{-5}
SXS:BBH:4417	24.102	6.780×10^{-3}	1.02×10^{-5}
SXS:BBH:4404	24.102	6.757×10^{-3}	1.02×10^{-5}
SXS:BBH:4418	24.102	6.735×10^{-3}	1.02×10^{-5}
SXS:BBH:4405	24.102	6.713×10^{-3}	1.02×10^{-5}
SXS:BBH:4419	24.102	6.691×10^{-3}	1.02×10^{-5}
SXS:BBH:4396	24.102	6.668×10^{-3}	1.02×10^{-5}
SXS:BBH:4420	24.102	6.646×10^{-3}	1.02×10^{-5}
SXS:BBH:4406	24.102	6.624×10^{-3}	1.02×10^{-5}
SXS:BBH:4421	24.102	6.602×10^{-3}	1.02×10^{-5}
SXS:BBH:4407	24.102	6.579×10^{-3}	1.02×10^{-5}
SXS:BBH:4422	24.102	6.557×10^{-3}	1.02×10^{-5}
SXS:BBH:4397	24.102	6.535×10^{-3}	1.02×10^{-5}

ORCID iDs

Peter James Nee https://orcid.org/0000-0002-2362-5420
Aldo Gamboa https://orcid.org/0000-0001-8391-5596
Harald P Pfeiffer https://orcid.org/0000-0001-9288-519X
Lorenzo Pompili https://orcid.org/0000-0002-0710-6778
Antoni Ramos-Buades https://orcid.org/0000-0002-6874-7421
Vijay Varma https://orcid.org/0000-0002-9994-1761
Michael Boyle https://orcid.org/0000-0002-5075-5116
Alessandra Buonanno https://orcid.org/0000-0002-5433-1409
Raffi Enficiaud https://orcid.org/0000-0003-3908-1912
Lawrence E Kidder https://orcid.org/0000-0001-5392-7342
Mark A Scheel https://orcid.org/0000-0001-6656-9134

References

[1] Abbott B P *et al* (KAGRA, LIGO Scientific, Virgo, VIRGO) 2018 *Living Rev. Relativ.* **21** 3
[2] Abbott B P *et al* (LIGO Scientific, Virgo) 2019 *Phys. Rev. X* **9** 031040
[3] Abbott R *et al* (LIGO Scientific, Virgo) 2021 *SoftwareX* **13** 100658
[4] Abbott R *et al* (LIGO Scientific, Virgo) 2021 *Phys. Rev. X* **11** 021053
[5] Abbott R *et al* (LIGO Scientific, VIRGO) 2021 arXiv:2108.01045
[6] Abbott R *et al* (LIGO Scientific, VIRGO, KAGRA) 2021 arXiv:2111.03606
[7] Abbott B P *et al* (LIGO Scientific, Virgo) 2019 *Astrophys. J. Lett.* **882** L24
[8] Venumadhav T, Zackay B, Roulet J, Dai L and Zaldarriaga M 2020 *Phys. Rev. D* **101** 083030
[9] Nitz A H, Kumar S, Wang Y F, Kastha S, Wu S, Schäfer M, Dhurkunde R and Capano C D 2021 arXiv:2112.06878
[10] Gupte N *et al* 2024 arXiv:2404.14286
[11] Punturo M *et al* 2010 *Class. Quantum Grav.* **27** 194002
[12] Reitze D *et al* 2019 *Bull. Am. Astron. Soc.* **51** 035 (arXiv:1907.04833)
[13] Amaro-Seoane P *et al* (LISA) 2017 arXiv:1702.00786
[14] Dhani A, Völkel S, Buonanno A, Estelles H, Gair J, Pfeiffer H P, Pompili L and Toubiana A 2024 arXiv:2404.05811
[15] Antonini F, Toonen S and Hamers A S 2017 *Astrophys. J.* **841** 77
[16] Kozai Y 1962 *Astron. J.* **67** 591–8
[17] Zevin M, Samsing J, Rodriguez C, Haster C-J and Ramirez-Ruiz E 2019 *Astrophys. J.* **871** 91
[18] Pompili L *et al* 2023 *Phys. Rev. D* **108** 124035
[19] Thompson J E, Hamilton E, London L, Ghosh S, Kolitsidou P, Hoy C and Hannam M 2024 *Phys. Rev. D* **109** 063012
[20] Nagar A *et al* 2018 *Phys. Rev. D* **98** 104052
[21] Varma V, Field S E, Scheel M A, Blackman J, Gerosa D, Stein L C, Kidder L E and Pfeiffer H P 2019 *Phys. Rev. Res.* **1** 033015
[22] Peters P C and Mathews J 1963 *Phys. Rev.* **131** 435–40
[23] Abac A G *et al* (LIGO Scientific, KAGRA, VIRGO) 2024 *Astrophys. J.* **973** 132
[24] Dhurkunde R and Nitz A H 2023 arXiv:2311.00242
[25] Gadre B, Soni K, Tiwari S, Ramos-Buades A, Haney M and Mitra S 2024 *Phys. Rev. D* **110** 044013
[26] Clarke T A, Romero-Shaw I M, Lasky P D and Thrane E 2022 *Mon. Not. R. Astron. Soc.* **517** 3778–84
[27] Portegies Zwart S F and McMillan S 2000 *Astrophys. J. Lett.* **528** L17
[28] Mandel I and O'Shaughnessy R 2010 *Class. Quantum Grav.* **27** 114007
[29] Samsing J, MacLeod M and Ramirez-Ruiz E 2014 *Astrophys. J.* **784** 71
[30] Rodriguez C L and Loeb A 2018 *Astrophys. J. Lett.* **866** L5
[31] Fragione G and Kocsis B 2018 *Phys. Rev. Lett.* **121** 161103
[32] Zevin M, Romero-Shaw I M, Kremer K, Thrane E and Lasky P D 2021 *Astrophys. J. Lett.* **921** L43
[33] Saini P, Favata M and Arun K G 2022 *Phys. Rev. D* **106** 084031
[34] Narayan P, Johnson-McDaniel N K and Gupta A 2023 *Phys. Rev. D* **108** 064003
[35] Shaikh M A, Bhat S A and Kapadia S J 2024 *Phys. Rev. D* **110** 024030
[36] Islam T, Varma V, Lodman J, Field S E, Khanna G, Scheel M A, Pfeiffer H P, Gerosa D and Kidder L E 2021 *Phys. Rev. D* **103** 064022
[37] Ramos-Buades A, Buonanno A and Gair J 2023 *Phys. Rev. D* **108** 124063
[38] Gamboa A *et al* 2024 arXiv:2412.12823
[39] Liu X, Cao Z and Zhu Z H 2023 arXiv:2310.04552
[40] Nagar A, Gamba R, Rettegno P, Fantini V and Bernuzzi S 2024 *Phys. Rev. D* **110** 084001
[41] Gamba R, Chiaramello D and Neogi S 2024 *Phys. Rev. D* **110** 024031
[42] Hinder I, Herrmann F, Laguna P and Shoemaker D 2010 *Phys. Rev. D* **82** 024033
[43] Mroue A H, Pfeiffer H P, Kidder L E and Teukolsky S A 2010 *Phys. Rev. D* **82** 124016
[44] Lewis A G M, Zimmerman A and Pfeiffer H P 2017 *Class. Quantum Grav.* **34** 124001
[45] Hinder I, Kidder L E and Pfeiffer H P 2018 *Phys. Rev. D* **98** 044015
[46] Huerta E A *et al* 2019 *Phys. Rev. D* **100** 064003
[47] Habib S and Huerta E A 2019 *Phys. Rev. D* **100** 044016
[48] Ramos-Buades A, Husa S, Pratten G, Estellés H, García-Quirós C, Mateu-Lucena M, Colleoni M and Jaume R 2020 *Phys. Rev. D* **101** 083015
[49] Healy J and Lousto C O 2022 *Phys. Rev. D* **105** 124010

[50] Ramos-Buades A, van de Meent M, Pfeiffer H P, Rüter H R, Scheel M A, Boyle M and Kidder L E 2022 *Phys. Rev. D* **106** 124040
[51] Wang H, Zou Y-C, Wu Q-W, Liu Y and Liu X 2024 *Phys. Rev. D* **109** 084063
[52] Wang H, Zou Y C, Wu Q W and Liu Y 2023 arXiv:2311.08822
[53] Wang H, Zou Y C, Wu Q W, Liu X and Li Z 2024 arXiv:2409.17636
[54] Knapp T, Chatziioannou K, Pfeiffer H, Scheel M A and Kidder L E 2024 arXiv:2410.02997
[55] Habib S, Scheel M and Teukolsky S 2024 arXiv:2410.05531
[56] Gamboa A, Khalil M and Buonanno A 2024 arXiv:2412.12831
[57] Mihaylov D P, Ossokine S, Buonanno A, Estelles H, Pompili L, Pürrer M and Ramos-Buades A 2023 arXiv:2303.18203
[58] Shaikh M A, Varma V, Pfeiffer H P, Ramos-Buades A and van de Meent M 2023 *Phys. Rev. D* **108** 104007
[59] SXS Collaboration 2025 SpEC: Spectral Einstein Code (available at: www.black-holes.org/SpEC.html)
[60] Kidder L E and Finn L S 2000 *Phys. Rev. D* **62** 084026
[61] Scheel M A, Boyle M, Chu T, Kidder L E, Matthews K D and Pfeiffer H P 2009 *Phys. Rev. D* **79** 024003
[62] Szilagyi B, Lindblom L and Scheel M A 2009 *Phys. Rev. D* **80** 124010
[63] Hemberger D A, Scheel M A, Kidder L E, Szilágyi B, Lovelace G, Taylor N W and Teukolsky S A 2013 *Class. Quantum Grav.* **30** 115001
[64] Lindblom L, Scheel M A, Kidder L E, Owen R and Rinne O 2006 *Class. Quantum Grav.* **23** S447–62
[65] Ossokine S, Kidder L E and Pfeiffer H P 2013 *Phys. Rev. D* **88** 084031
[66] Rinne O 2006 *Class. Quantum Grav.* **23** 6275–300
[67] Rinne O, Lindblom L and Scheel M A 2007 *Class. Quantum Grav.* **24** 4053–78
[68] Pfeiffer H P, Kidder L E, Scheel M A and Teukolsky S A 2003 *Comput. Phys. Commun.* **152** 253–73
[69] Ossokine S, Foucart F, Pfeiffer H P, Boyle M and Szilágyi B 2015 *Class. Quantum Grav.* **32** 245010
[70] York J J W 1999 *Phys. Rev. Lett.* **82** 1350–3
[71] Pfeiffer H P and York J J W 2003 *Phys. Rev. D* **67** 044022
[72] Cook G B and Pfeiffer H P 2004 *Phys. Rev. D* **70** 104016
[73] Lovelace G 2009 *Class. Quantum Grav.* **26** 114002
[74] Boyle M, Brown D A, Kidder L E, Mroue A H, Pfeiffer H P, Scheel M A, Cook G B and Teukolsky S A 2007 *Phys. Rev. D* **76** 124038
[75] Pfeiffer H P, Brown D A, Kidder L E, Lindblom L, Lovelace G and Scheel M A 2007 *Class. Quantum Grav.* **24** S59–82
[76] Buchman L T, Pfeiffer H P, Scheel M A and Szilagyi B 2012 *Phys. Rev. D* **86** 084033
[77] Buonanno A, Kidder L E, Mroue A H, Pfeiffer H P and Taracchini A 2011 *Phys. Rev. D* **83** 104034
[78] Purrer M, Husa S and Hannam M 2012 *Phys. Rev. D* **85** 124051
[79] Ramos-Buades A, Husa S and Pratten G 2019 *Phys. Rev. D* **99** 023003
[80] Habib S, Ramos-Buades A, Huerta E A, Husa S, Haas R and Etienne Z 2021 *Class. Quantum Grav.* **38** 125007
[81] Radia M, Sperhake U, Berti E and Croft R 2021 *Phys. Rev. D* **103** 104006
[82] Carullo G, Albanesi S, Nagar A, Gamba R, Bernuzzi S, Andrade T and Trenado J 2024 *Phys. Rev. Lett.* **132** 101401
[83] Buonanno A and Damour T 2000 *Phys. Rev. D* **62** 064015
[84] Buonanno A, Chen Y and Damour T 2006 *Phys. Rev. D* **74** 104005
[85] Pretorius F 2005 *Phys. Rev. Lett.* **95** 121101
[86] Campanelli M, Lousto C O, Marronetti P and Zlochower Y 2006 *Phys. Rev. Lett.* **96** 111101
[87] Baker J G, Centrella J, Choi D-I, Koppitz M and van Meter J 2006 *Phys. Rev. Lett.* **96** 111102
[88] Buonanno A, Cook G B and Pretorius F 2007 *Phys. Rev. D* **75** 124018
[89] Damour T and Nagar A 2007 *Phys. Rev. D* **76** 044003
[90] Damour T, Nagar A and Villain L 2014 *Phys. Rev. D* **89** 024031
[91] Nagar A, Damour T and Tartaglia A 2007 *Class. Quantum Grav.* **24** S109–24
[92] Jiménez-Forteza X, Keitel D, Husa S, Hannam M, Khan S and Pürrer M 2017 *Phys. Rev. D* **95** 064024
[93] Hofmann F, Barausse E and Rezzolla L 2016 *Astrophys. J. Lett.* **825** L19

[94] Julié F L, Pompili L and Buonanno A 2024 arXiv:2406.13654
[95] Ramos-Buades A, Buonanno A, Khalil M and Ossokine S 2022 *Phys. Rev. D* **105** 044035
[96] Knee A M, Romero-Shaw I M, Lasky P D, McIver J and Thrane E 2022 *Astrophys. J.* **936** 172
[97] Bonino A, Schmidt P and Pratten G 2024 arXiv:2404.18875
[98] Sun Y and Price R H 1988 *Phys. Rev. D* **38** 1040–52
[99] Boyle M *et al* 2019 *Class. Quantum Grav.* **36** 195006
[100] Strande S *et al* 2021 Expanse: computing without boundaries: architecture, deployment and early operations experiences of a supercomputer designed for the rapid evolution in science and engineering *Practice and Experience in Advanced Research Computing 2021: Evolution Across All Dimensions (PEARC '21)* (Association for Computing Machinery) (https://doi.org/10.1145/3437359.3465588)